Ce doped polyaniline nanoparticles for absorption and photoacoustic imaging response to GSH *in vitro* and *in vivo*

Yulin Kuang [a,b,c,1], Nanbo Liu [c,1], Sheng Ye [b,1], Xiang Li [d], Xuyuan Chen [a], Li Qi [b], Ping Zhu [c,**], Ruiyuan Liu [b,*], Xu Wu [a,***]

[a] *Department of Thoracic Surgery, Nanfang Hospital, Southern Medical University, Guangzhou, Guangdong, 510515, China*
[b] *Guangdong Provincial Key Laboratory of Medical Image Processing, School of Biomedical Engineering, Southern Medical University, Guangzhou, Guangdong, 510515, China*
[c] *Guangdong Cardiovascular Institute, Guangdong Provincial People's Hospital, Guangdong Academy of Medical Sciences, Guangzhou, Guangdong, 510100, China*
[d] *Emergency Department, Nanfang Hospital, Southern Medical University, Guangzhou, Guangdong, 510515, China*

ARTICLE INFO

ABSTRACT

Glutathione (GSH) is an important biological thiol in cells, which is involved in many physiological processes in the organism and regulates pathological processes of cells. Rapid and accurate monitoring of GSH *in vitro* and *in vivo* is quite needed in investigating important biochemical events. In this contribution, innovative cerium (Ce) doped polyaniline (Ce–Fe@PANI NPs) were prepared *via* Fe(III) induced oxidization polymerization method. Upon addition of GSH, the absorption of Ce–Fe@PANI NPs red shifted from the visible to the NIR region, confirming the excellent absorption response to GSH. Moreover, Ce–Fe@PANI NPs exhibited excellent photoacoustic (PA) imaging enhancement in tube and shifted the PA intensity peak from 680 nm to 820 nm upon addition of GSH. *In vitro* and *in vivo* experiment verified that Ce–Fe@PANI NPs can monitor GSH in deep tissues *via* PA imaging technology. Collectively, this research provides Ce–Fe@PANI NPs would serve as a powerful nanoplatform to realize PA imaging detection of GSH *in vitro* and *in vivo*.

1. Introduction

Glutathione (GSH) is an important biological thiol in cells, which is involved in many physiological processes in the organism and regulates many pathological processes of cells [1–3]. For example, GSH can maintain intracellular redox states, influence intracellular signal transduction, regulate gene expression, and so on [4–6]. Abnormal concentration of GSH can induce various diseases including liver damage, Alzheimer's disease, and brain injure [7–9]. Moreover, the different level in GSH between cancer cells and normal cells is reported to be one of the most important physiological indicators for cancer diagnosis [10, 11]. Therefore, it is very important to monitor GSH in organisms or in cells. To date, various approaches are utilized to detect GSH, including mass spectrometry, liquid chromatography, capillary electrophoresis, absorption/emission spectroscopy, and surface enhanced Raman scattering [12–15]. However, these methods can not be applied to monitor GSH in deep tissues *in vitro* and *in vivo* [16].

Photoacoustic (PA) imaging is an innovative imaging technology which combinate photo-excitation and ultrasonic detection [17,18]. PA imaging can provide the tissues imaging with deeper tissue penetration, excellent contrast, super spatial resolution, and strong sensitivity [19, 20]. Hence, PA imaging technique has garnered enormous attention in recent years and is applied in biomedical research and diseases diagnosis [21–25]. Recently, various NIR absorption materials, such as small organic molecules [26,27], gold nanoparticles [28,29], carbon nanoparticles [30,31], 2D materials [32,33], sulfides [34], and conjugated polymers [35], have been exploited for PA imaging to monitor biomolecular and cancer diagnosis. Among these NIR absorption materials, with the advantages of ease synthesis and modification, excellent biocompatibility, and large absorption coefficient, metal ion doped

polyanilines have attracted much attention for PA imaging [36,37].

However, the PA intensity peak from most NIR absorption materials kept stable, which can only exhibit the "turn on/off" PA signal for monitoring biomolecular in organism. Hence, NIR absorption materials, which demonstrated absorption response to GSH, may produce different PA signal according to the photo wavelength and induce the shift of PA intensity peak. Furthermore, visualization of GSH at the molecular level in deep tissues *in vivo* can monitor disease state and dynamically track the course of disease. However, report on the fabrication and development of NIR absorption materials which demonstrated PA response to GSH are scarce to date. Considering the merits, such as real-time detection capacity, deeper tissues penetration, and tracking the pathological processes at the molecular level, development of GSH responsive NIR absorption materials for PA imaging is of very importance to conduct biomedical research.

In this contribution, we designed and fabricated Ce doped polyaniline with Fe(III) induced oxidization polymerization methods for monitoring of GSH in deep tissues, which was denominated as Ce–Fe@PANI NPs (Scheme 1). Ce–Fe@PANI NPs could interact with GSH and induce a red shift in the absorption spectrum from the visible to the NIR region. Ce–Fe@PANI NPs exhibited high biocompatibility, excellent biosafety, and absorption response to GSH. Moreover, Ce–Fe@PANI NPs demonstrated PA enhancement in tube and shifted the PA intensity peak from 680 nm to 820 nm upon addition of GSH. *In vitro* and *in vivo* experiment confirmed that Ce–Fe@PANI NPs can monitor GSH in deep tissues *via* PA imaging technology. Collectively, this research provides Ce–Fe@PANI NPs would serve as a powerful nanoplatform to realize PA imaging detection of GSH *in vitro* and *in vivo*.

2. Materials and methods

2.1. Instruments

Particle size was detected by ZetasizerNano ZS (Malvern Panalytical, UK). Transmission electron microscopy (TEM) was obtained from PHILIPS TECNAI 10. UV–vis absorption spectra were measured *via* the Thermofisher Evolution 300 spectropolarimeter. Photoacoustic images were captured with an MSOT system (iThera Medical, Germany). Infrared spectrum was captured by VerTEX 70 (Bruker, Germany). The XRD was obtained by D8 ADVANCE (Bruker, Germany). The XPS was provided by Kratos Axis Ulra DLD (Kratos, UK). ICP-MS was carried out in ThermoFisher TQ-ICP-MS.

2.2. Construction of Ce–Fe@PANI NPs

The preparation method of Ce–Fe@PANI NPs was as follows. Firstly, $FeCl_3$ (80 mg), $CeCl_3$ (30 mg), and BSA (70 mg) was dissolved in

deionized water (10 mL). Secondly, hydrochloric acid (95 mL, 36% by mass) and aniline (95 mL) were added into deionized water (1 mL) to prepare aniline/HCl solution. Thirdly, aniline/HCl solution drop added into the Ce–Fe@BSA complex solution at 4 °C and last for 10h. Finally, the Ce–Fe@PANI NPs were obtained by centrifugation.

For the control experiment, Fe@PANI NPs was were synthesized using $FeCl_3$ (100 mg), BSA (70 mg), and aniline/HCl solution as the precursor. The Ce@PANI NPs was were synthesized using $CeCl_3$ (100 mg), BSA (70 mg), and aniline/HCl solution as the precursor.

2.3. Absorption response Ce–Fe@PANI NPs to GSH in tube

A typical experimental procedure was as follows: the stock solutions of Ce–Fe@PANI NPs (PBS, 750 μg/mL) was prepared in a 10 mLvolumetric flask. 1 mL stock solution of Ce–Fe@PANI NPs (750 μg/mL) and 1 mL GSH solution (0, 0.5, 1, 1.5, 2, 2.5, 3, 3.5, 4, 4.5, 5 mM) were transferred to a 10 mL volumetric flask and diluted to volume with PBS solution. The final sample contains Ce–Fe@PANI NPs (75 μg/mL) and GSH (0, 0.05, 0.1, 0.15, 0.2, 0.25, 0.3, 0.35, 0.4, 0.45, 0.5 mM). The absorption spectra were recorded after incubation at room temperature after 30 min.
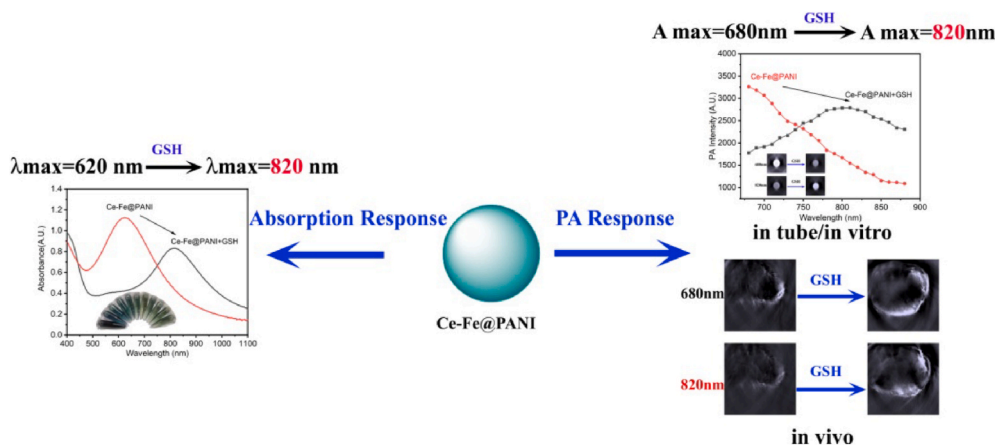
2.4. PA response of Ce–Fe@PANI NPs to GSH in tube

For PA detection in tube, the samples containing Ce–Fe@PANI NPs (75 μg/mL) and GSH (0, 0.05, 0.1, 0.15, 0.2, 0.25, 0.3, 0.35, 0.4, 0.45, 0.5 mM) were prepared and kept at room temperature for 30 min. PA imaging was carried out on a multispectral optoacoustic tomography (MSOT) in Vision 256-TF small animal scanner (iThera Medical GmbH, Munich, Germany).

2.5. PA response of Ce–Fe@PANI NPs to GSH in vitro

4T1 or L929 cells (2×10^6) were seeded in a 75 cm^2 culture bottle. The cells were divided into three groups, including (1) control. (2) Ce–Fe@PANI: the cells were incubated with Ce–Fe@PANI NPs (100 μg/mL) for 3 h (3) Ce–Fe@PANI + GSH: the cells were incubated with Ce–Fe@PANI NPs (100 μg/mL) for 3 h, then incubated with GSH (10 mM) for 0.5 h. The cells in three groups were washed with PBS buffer, digested with trypsin and centrifuged, resuspended with 0.5% agarose solution. After cooling, the PA image was observed by the MSOT system.

2.6. PA response of Ce–Fe@PANI NPs to GSH in vivo

The normal mice were in anesthesia and placed in prone position. After injection of Ce–Fe@PANI NPs (100 μL, 1 mg/mL) into the muscle in the hind leg of normal mice, the PA images of muscle tissues were

Scheme 1. The absorption and PA response of Ce–Fe@PANI NPs to GSH *in vitro* and *in vivo*.

captured to investigate the PA enhancement of Ce–Fe@PANI NPs. After injection of Ce–Fe@PANI NPs (100 μL, 1 mg/mL) into the muscle in the hind leg of normal mice, GSH (100 μL, 50 mM) was intravenous injection and the PA images of muscle tissues was monitored to evaluate the PA response of Ce–Fe@PANI NPs to GSH.

4T1 tumor-bearing mice were in anesthesia and placed in prone position. After intratumoral injection of Ce–Fe@PANI NPs (100 μL, 1 mg/mL), the PA images of tumor area were captured to exploit the PA response of Ce–Fe@PANI NPs to GSH in tumor.

3. Result and discussion

3.1. The preparation and property of Ce–Fe@PANI NPs

Ce–Fe@PANI NPs were prepared by Fe(III) induced oxidative chemical polymerization of aniline using bovine serum albumin (BSA) as stability agents under $CeCl_3$ (Fig. 1A). In a typical synthetic process, $FeCl_3$, $CeCl_3$, and BSA were mixed in water, then the aniline/HCl solution was added. The reaction was carried out at 4 °C for 10h. The mixtures were centrifuged to remove large particles and obtain Ce–Fe@PANI NPs. The structures were confirmed by IR spectra, XRD, XPS, and ICP-MS (Fig. S1-S3). The peaks at 883 and 905 eV were observed in the XPS spectra of Ce–Fe@PANI NPs, which correspond to the electron energy peaks of Ce 3d5/2 and 3d3/2, respectively. It seems that the valence state of Ce is III. Moreover, the XPS spectra of Ce–Fe@PANI NPs exhibited peaks at 709 and 725 eV, which are ascribed to the electron energy peaks of Fe 2p3/2 and 2p1/2, respectively, confirming that the valence state of Fe is II. The Fe^{2+} and Ce^{3+} concentration in Ce–Fe@PANI NPs (10 mg/mL) was determined to be 0.248 mM and 0.0951 mM, respectively.

Ce–Fe@PANI NPs were highly dispersed and stable in water or PBS, which were blue. The morphologies of Ce–Fe@PANI NPs were characterized using transmission electron microscopy (TEM) and dynamic light scattering (DLS) (Fig. 1B and C). The average hydrodynamic size of Ce–Fe@PANI NPs was determined to be 178 nm with *zeta* potential about 24 mV (Fig. 1D). Moreover, no aggregation or precipitation was observed in Ce–Fe@PANI NPs PBS solution for 20 days (Fig. S4), confirming excellent stability.

3.2. Absorption response of Ce–Fe@PANI NPs to GSH

We first measured the absorption spectrum of Ce–Fe@PANI NPs upon addition of GSH to investigate the responsive property of Ce–Fe@PANI NPs. As shown in Fig. 2A and **B**, Ce–Fe@PANI NPs exhibited absorption peak around 620 nm in PBS. Upon addition of GSH, the UV peak value was red-shifted from visible region (620 nm) to NIR region (820 nm), in consort with the absorbance decrease. Accompanied with the red shift of absorbance, the color of Ce–Fe@PANI NPs solution shifted from blue to black green. On the other hand, in the extremely low concentration ranged 0–0.2 mM, the ratio between absorption intensity around 820 nm (A_{820}) and absorption intensity around 620 nm(A_{620}) enhanced linearly with the concentration of GSH (R = 0.9982) (Fig. 2C, insert), which was capable of quantitative determination of GSH.

In contrast to the absorption shift response to GSH, Ce–Fe@PANI NPs exhibited absorption stability to various biologically species. As shown in Fig. 2D, negligible changes were observed in the A_{820}/A_{620} of Ce–Fe@PANI NPs with other component such as amino acids, KCl, KI, KF, KIO_3, H_2O_2, K_2SO_3, K_2SO_4, KHS, and K_2S. In addition, in the present of GSH, A_{820}/A_{620} enhanced 1.76, which indicated that Ce–Fe@PANI NPs exhibit absorption response to GSH.

The Fe(III) could be acted as an oxidant to polymerize aniline [38]. We synthesized Fe dopped polyaniline (Fe@PANI) and Ce dopped polyaniline (Ce@PANI) to investigate the absorption response to GSH. As shown in Fig. S5, the color of the Fe@PANI solutions was blue with a max absorption peak around 620 nm and changed slightly upon addition of 0.5 mM GSH. To our surprise, the Ce@PANI solution exhibited pale yellow color. Moreover, upon addition of GSH, the absorption spectrum of the Ce@PANI changed slightly. This implied that Ce and Fe doping in Ce–Fe@PANI NPs was important for the response to GSH. It has been reported that PANI exists in two forms including the emeraldine base (EB) and emeraldine salt (ES). Upon doping with acids or transition metals, EB PANI can convert to ES PANI which demonstrated strong NIR absorption [39–41]. We also measured IR spectra of Ce–Fe@PANI NPs after treatment with GSH. As shown in Fig. S1, upon addition of GSH, the C–C peak from PANI shifted from 1148 cm^{-1} to 1136 cm^{-1}, confirming the interaction between the PANI and GSH. Thus, the interaction between GSH with Ce–Fe@PANI NPs could facilitate the generation of ES PANI, thereby inducing the red shift of the absorption spectrum.
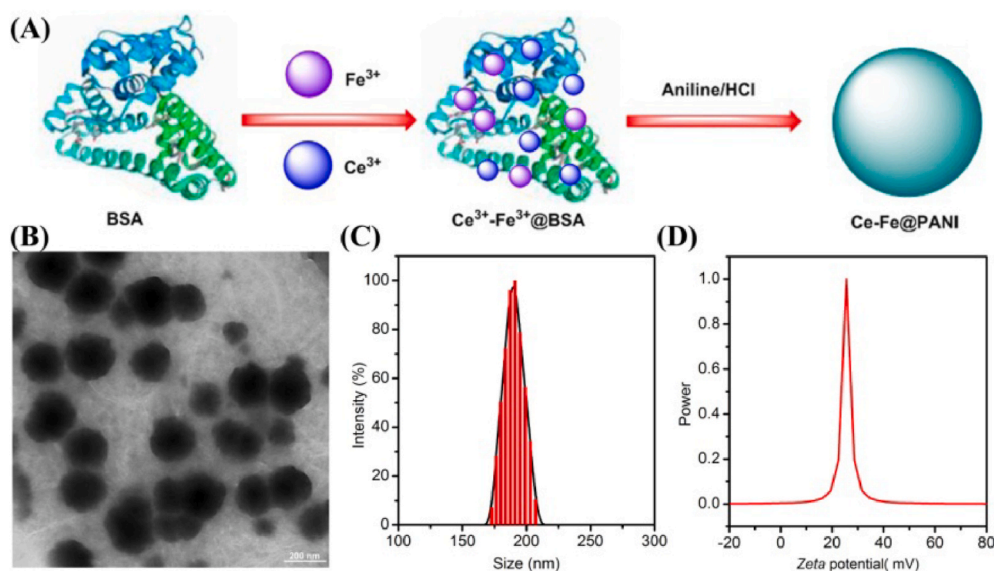

Fig. 1. Synthesis and Characterization of Ce–Fe@PANI NPs. (A) The preparation of Ce–Fe@PANI NPs. (B) The TEM imaging of Ce–Fe@PANI NPs. (C) The DLS of Ce–Fe@PANI NPs. (D) The *zeta* potential of Ce–Fe@PANI NPs.
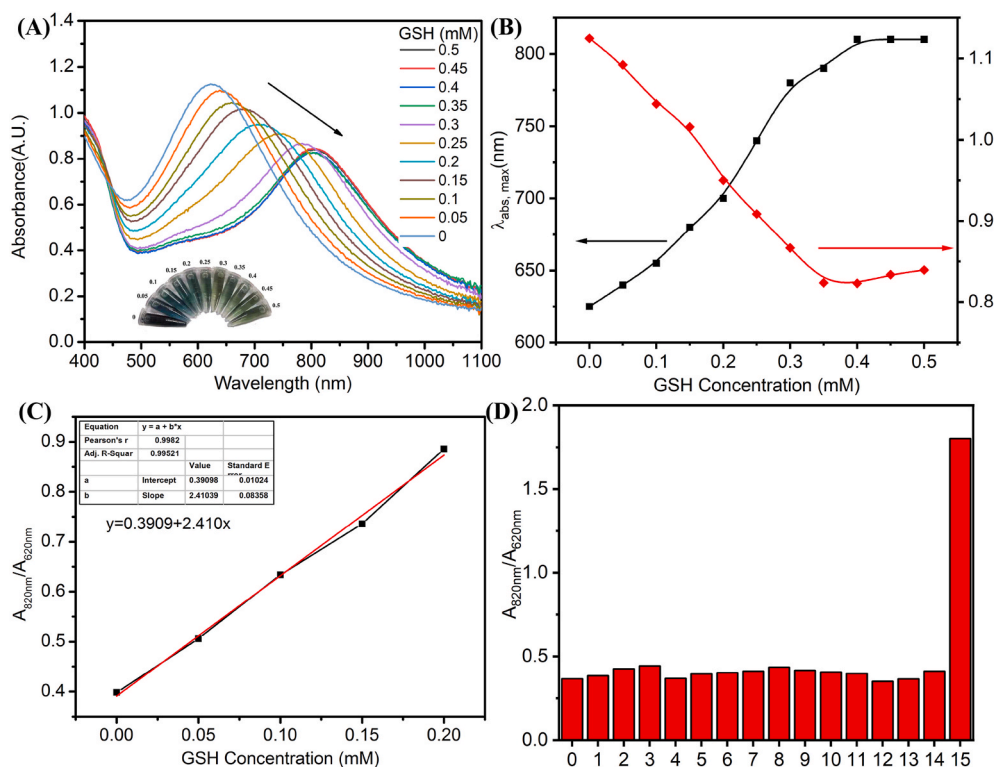
Fig. 2. The NIR absorption response of Ce–Fe@PANI NPs to GSH. (A) The absorption spectrum of Ce–Fe@PANI NPs (75 µg/mL) upon addition of GSH. (B) The absorption maximum and absorbance of Ce–Fe@PANI NPs (75 µg/mL) upon addition of GSH. (C) The relation between absorption ratio at 820 nm/620 nm between GSH concentration. (D)Absorption ratio at 820 nm/620 nm of the Ce–Fe@PANI NPs solution in the presence of different distractors (at 1.0 mM each) in PBS 1: phenylalanine; 2: histidine; 3: threonine; 4: tryptophan; 5: lysine; 6: KCl; 7: KI; 8: KF; 9: KIO_3; 10: H_2O_2; 11: K_2SO_3; 12: K_2SO_4; 13: KHS; 14: K_2S, 15: GSH.

3.3. PA response of Ce–Fe@PANI NPs to GSH in tube

Inspired by the excellent absorption response of Ce–Fe@PANI NPs to GSH, we wonder the PA response of Ce–Fe@PANI NPs to GSH in tube.

We first investigated the PA imaging of Ce–Fe@PANI NPs upon addition of GSH. Ce–Fe@PANI NPs exhibited maximum PA intensity around 680 nm. Upon addition of GSH, the PA intensity at 680 nm decreased, accompanied with the enhancement of PA intensity at 820 nm.
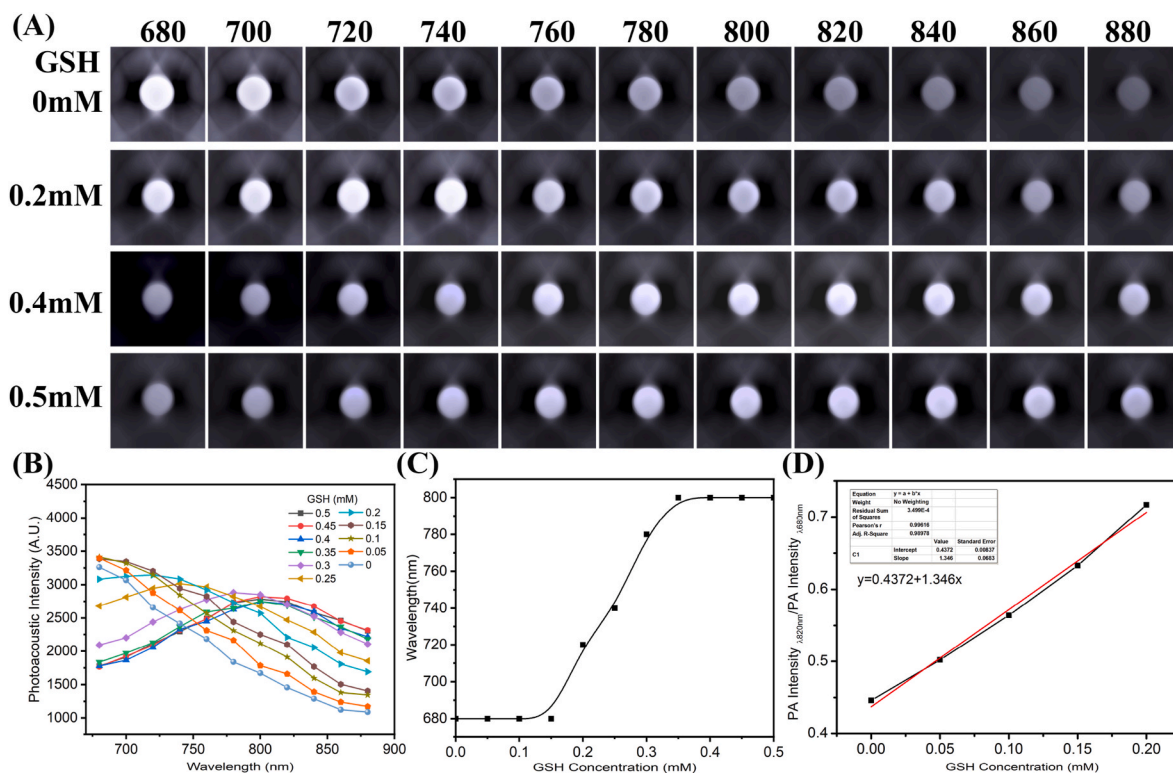

Fig. 3. (A) The photoacoustic imaging of Ce–Fe@PANI NPs upon addition of GSH. (B) The photoacoustic intensity of Ce–Fe@PANI NPs (75 µg/mL) upon addition of GSH. (C) The relation of photoacoustic intensity peak wavelength with GSH concentration. (D)The relation between photoacoustic intensity ratio at 820 nm/680 nm with GSH concentration.

Moreover, the PA intensity peak value was red-shifted from 680 nm to 820 nm, while the concentration of GSH increased from 0 to 0.5 mM (Fig. 3A–C and **S6**). To our surprise, the ratio between PA intensity around 820 nm ($A_{\lambda\,=\,820nm}$) and PA intensity around 680 nm ($A_{\lambda\,=\,680nm}$) was found to be linearly correlated with the concentration of GSH arranged from 0 to 0.2 mM. The PA intensity ratio was determined to be linearly correlated with GSH concentration, which followed linear regression equation: $A_{\lambda\,=\,820nm}/A_{\lambda\,=\,680nm} = 1.346C_{GSH}+0.4372$, $R_2 = 0.99616$ (Fig. 3D, insert), which was capable of quantitative determination of GSH.

3.4. PA response of Ce–Fe@PANI NPs to GSH in vitro

The cytotoxicity of Ce–Fe@PANI NPs was firstly investigated by standard CCK-8 assay in tumor cells (4T1 cells) and normal cells (L929 cells and 293T cells). As shown in Fig. S7, the viability of cells was higher than 70% after incubation with 100 µg/mL of Ce–Fe@PANI NPs for 24 h, demonstrating that Ce–Fe@PANI NPs is biocompatible to live cells.

To explore PA response of Ce–Fe@PANI NPs to GSH *in vitro*, we first measured the PA signal in 4T1 tumor cells at 680 nm or 820 nm. The 4T1 cells were divided to three groups: 4T1 cell (control group), 4T1 cells incubated with Ce–Fe@PANI NPs (Ce–Fe@PANI group), and 4T1 cells stained with Ce–Fe@PANI NPs then with GSH (Ce–Fe@PANI + GSH). As shown in Fig. 4A–B, both of 4T1 cells in Ce–Fe@PANI group and in Ce–Fe@PANI + GSH group revealed strong PA signal at 680 nm or 820 nm, compare with the control group, which confirmed the excellent PA enhancement of Ce–Fe@PANI NPs *in vitro*. To our surprise, the PA intensity at 680 nm in 4T1 cells decreased upon addition of GSH. On the contrary, incubated with GSH, 4T1 cells enhanced the intensity of PA signal at 820 nm.

Then, we incubated the normal cells with Ce–Fe@PANI NPs and measured the PA imaging (Fig. S8). The results showed that L929 cells generated higher PA intensity at 680 nm compare with 4T1 cells, while the PA intensity at 820 nm of L929 cells was lower than that of 4T1 cells (Fig. S9). It seems that GSH with higher concentration in 4T1 tumor cells interact with Ce–Fe@PANI NPs, resulting in higher PA intensity compare to normal cells with lower GSH concentration. However, upon addition of GSH, the PA signals at 820 nm or 680 nm from tumor and normal cells exhibited little difference (Fig. S10). All these results confirmed that GSH in the tumor microenvironment could alter the PA intensity of Ce–Fe@PANI NPs.

3.5. PA response of Ce–Fe@PANI NPs to GSH in vivo

Encouraged by the excellent PA imaging of Ce–Fe@PANI NPs *in vitro*, we next evaluated the *in vivo* PA imaging performance. We first administrated Ce–Fe@PANI NPs into muscle in the hinder leg of mice, and recorded the PA signal in the muscle tissues. As shown in Fig. S11, the brightest PA signal was observed at 680 nm, while the PA signal decreased with increase of photo wavelength. The result was accompanied with the absorption response of Ce–Fe@PANI NPs. Moreover, after injection of Ce–Fe@PANI NPs in muscles tissues, the PA intensity at 680 nm reached its highest value within 35min (Fig. 5A). Then, with time lapse, the PA signal at 680 nm in muscle tissues gradually weakened, but the corresponding PA signal can be detected after 120min. We then recorded the PA imaging at muscle tissues with administration of Ce–Fe@PANI NPs after intravenous injection of GSH. Strongest PA intensity was achieved under the 820 nm laser irradiation after GSH administration (Fig. S12). Furthermore, maximum PA intensity at 820 nm was observed after injection of GSH for 40min (Fig. 5B). To our surprise, PA signal at 820 nm still can be monitored after injection GSH for 120 min.

Inspired by the photoacoustic response of Ce–Fe@PANI NPs to GSH in muscle tissues, Ce–Fe@PANI NPs were intratumoral injected into the 4T1 tumor-bearing mouse. Next, the PA signal in tumor tissues was investigated at 680 nm or 820 nm. As demonstrated in Fig. 6A, PA signal at 680 nm in tumor site was observed, and its highest intensity was achieved within 1.5 h. Although the PA intensity at 680 nm gradually faded with time lapse, the corresponding PA signal in the tumor site could be monitored even after 12 h. Moreover, the PA signal at 820 nm in tumor site can also be observed (Fig. 6B). To our surprise, PA signals at 820 nm increased and reached its highest value around 2h, which is later than PA intensity at 680 nm (Fig. S13). It seems that Ce–Fe@PANI NPs accumulated in the tumor interact with GSH in tumor microenvironments, which resulting in absorption red shift accompanied with that PA intensity peak alters from 680 to 820 nm. The above results demonstrated that efficient monitoring of GSH in tumor could be achieved through investigation the PA imaging from Ce–Fe@PANI NPs.

3.6. Biosafety assessment

The potential damage of Ce–Fe@PANI NPs was explored through H&E staining of histological slices from organs on day 14, including heart, lung, liver, spleen, and kidney. As exhibited in Fig. S14, no obvious signs of organ damage were observed after administration of Ce–Fe@PANI NPs, which indicates that Ce–Fe@PANI NPs treatment has no obvious side effects. Moreover, Ce–Fe@PANI NPs at different dosages were intravenously injected into normal BALB/c mice. The mice body weight exhibited no dramatic change during the observation period, verifying a weak adverse effect on mice growth after intravenous injection of Ce–Fe@PANI NPs (Fig. S15). On the other hand, blood panel analysis was carried out on day 14 after administration of Ce–Fe@PANI NPs (Fig. S16). The concentration of hemoglobin (HGB), alanine
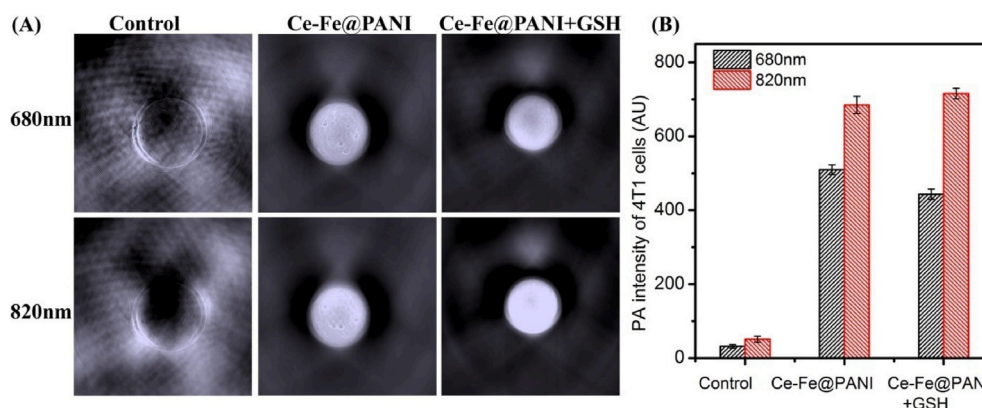

Fig. 4. (A) The PA imaging at 680 nm or 820 nm of 4T1 cells incubated with Ce–Fe@PANI NPs and GSH. (B) The PA intensity at 680 nm or 820 nm of 4T1 cells stained with Ce–Fe@PANI NPs and GSH (n = 3).
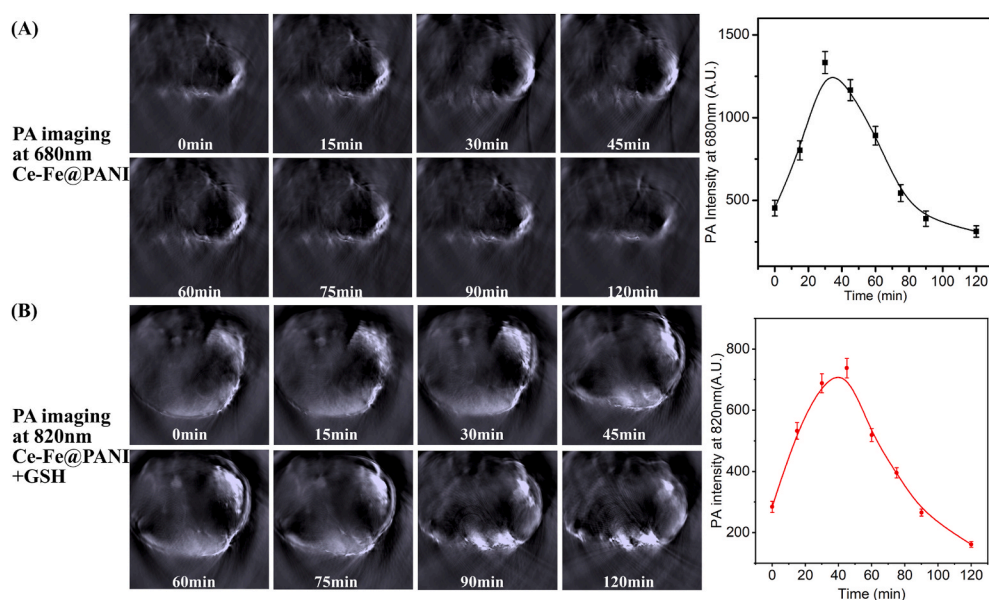
Fig. 5. (A) The photoacoustic imaging and intensity of the muscle tissues at 680 nm after injection of Ce–Fe@PANI NPs. (B) The photoacoustic imaging and intensity of the muscle tissues at 820 nm after injection of Ce–Fe@PANI NPs then GSH (n = 3).
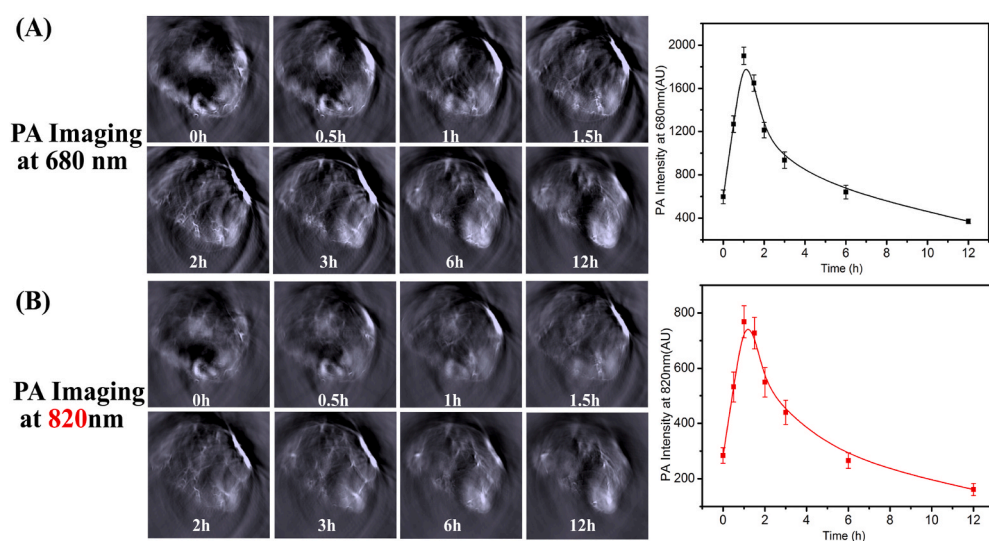

Fig. 6. (A) The photoacoustic imaging and intensity of the tumor at 680 nm after injection of Ce–Fe@PANI NPs (n = 3). (B) The photoacoustic imaging and intensity of the tumor at 820 nm after injection of Ce–Fe@PANI NPs (n = 3).

aminotransferase (ALT), aspartate transaminase (AST), white blood cells (WBC), Platelet count (PLT), and creatinine (CR) were within the normal ranges. Herein, all the these findings confirmed the excellent biosecurity of Ce–Fe@PANI NPs.

4. Conclusion

In this contribution, innovative Ce doped PANI nanoparticle (Ce–Fe@PANI NPs) was prepared *via* Fe(III) induced oxidization polymerization method. Ce–Fe@PANI NPs could interact with GSH and demonstrated a red shift in the absorption spectrum from the visible to the NIR region, which exhibited absorption response to GSH. Furthermore, Ce–Fe@PANI NPs exhibited great photoacoustic imaging enhancement and PA response to GSH in tube and *in vitro*. *In vivo* experiment verified the PA response of Ce–Fe@PANI NPs to GSH. Overall, this Ce–Fe doped PANI nanoplatform enjoys absorption and PA response to GSH, which is suitable for detection GSH in deep tissues *in vitro* and *in vivo*.

CRediT authorship contribution statement

Yulin Kuang: Conceptualization, Methodology. **Nanbo Liu:** Conceptualization, Methodology. **Sheng Ye:** Conceptualization, Methodology. **Xiang Li:** Validation. **Xuyuan Chen:** Validation. **Li Qi:** Methodology. **Ping Zhu:** Supervision, Project administration. **Ruiyuan Liu:** Writing – review & editing. **Xu Wu:** Supervision, Project administration.

Declaration of competing interest

The authors declare that they have no known competing financial interests or personal relationships that could have appeared to influence the work reported in this paper.

Appendix A. Supplementary data

Supplementary data to this article can be found online at https://doi.org/10.1016/j.bioactmat.2022.01.022.

References

[1] S. Singh, A.R. Khan, A.K. Gupta, Role of glutathione in cancer pathophysiology and therapeutic interventions, J. Exp. Therapeut. Oncol. 9 (2012) 303–316.

[2] G.K. Balendiran, R. Dabur, D. Fraser, The role of glutathione in cancer, Cell Biochem. Funct. 22 (2004) 343–352.

[3] A. Bansal, M.C. Simon, Glutathione metabolism in cancer progression and treatment resistance, J. Cell Biol. 217 (2018) 2291–2298.

[4] J.R. Prigge, L. Coppo, S.S. Martin, F. Ogata, C.G. Miller, M.D. Bruschwein, D. J. Orlicky, C.T. Shearn, J.A. Kundert, J. Lytchier, A.E. Herr, Å. Mattsson, M. P. Taylor, T.N. Gustafsson, E.S.J. Arnér, A. Holmgren, E.E. Schmidt, Hepatocyte hyperproliferation upon liver-specific Co-disruption of Thioredoxin-1, Thioredoxin Reductase-1, and glutathione Reductase, Cell Rep. 19 (2017) 2771–2781.

[5] P. Diaz-Vivancos, A. de Simone, G. Kiddle, C.H. Foyer, Glutathione–linking cell proliferation to oxidative stress, Free Radic. Biol. Med. 89 (2015) 1154–1164.

[6] J.Y. Cao, A. Poddar, L. Magtanong, J.H. Lumb, T.R. Mileur, M.A. Reid, C.M. Dovey, J. Wang, J.W. Locasale, E. Stone, S.P.C. Cole, J.E. Carette, S.J. Dixon, A genome-wide haploid genetic screen identifies regulators of glutathione abundance and ferroptosis sensitivity, Cell Rep. 26 (2019) 1544–1556.

[7] I. Finamor, S. Pérez, C.A. Bressan, C.E. Brenner, S. Rius-Pérez, P.C. Brittes, G. Cheiran, M.I. Rocha, M. da Veiga, J. Sastre, M.A. Pavanato, Chronic aspartame intake causes changes in the trans-sulphuration pathway, glutathione depletion and liver damage in mice, Redox Biol. 11 (2017) 701–707.

[8] P.K. Mandal, S. Saharan, M. Tripathi, G. Murari, Brain glutathione levels–a novel biomarker for mild cognitive impairment and Alzheimer's disease, Biol. Psychiatr. 78 (2015) 702–710.

[9] L.K. Mischley, K.E. Conley, E.G. Shankland, T.J. Kavanagh, M.E. Rosenfeld, J. E. Duda, C.C. White, T.K. Wilbur, P.U. De La Torre, J.M. Padowski, Central nervous system uptake of intranasal glutathione in Parkinson's disease, NPJ Parkinsons Dis. 2 (2016) 16002.

[10] D.Y.-K. Wong, Y.-L. Hsiao, C.-K. Poon, P.-C. Kwan, S.-Y. Chao, S.-T. Chou, C.-S. Yang, Glutathione concentration in oral cancer tissues, Cancer Lett. 81 (1994) 111–116.

[11] S. Singh, A.R. Khan, A.K. Gupta, Role of glutathione in cancer pathophysiology and therapeutic interventions, J. Exp. Therapeut. Oncol. 9 (2012) 303–316.

[12] C. Wei, X. Liu, Y. Gao, Y. Wu, X. Guo, Y. Ying, Y. Wen, H. Yang, Thiol-disulfide exchange reaction for cellular glutathione detection with surface-enhanced Raman scattering, Anal. Chem. 90 (2018) 11333–11339.

[13] J. Vacek, B. Klejdus, J. Petrlová, L. Lojková, V. Kubán, A hydrophilic interaction chromatography coupled to a mass spectrometry for the determination of glutathione in plant somatic embryos, Analyst 131 (2006) 1167–1174.

[14] W. Chen, Y. Zhao, T. Seefeldt, X. Guan, Determination of thiols and disulfides via HPLC quantification of 5-thio-2-nitrobenzoic acid, J. Pharm. Biomed. Anal. 48 (2008) 1375–1380.

[15] Y. Xianyu, Y. Xie, N. Wang, Z. Wang, X. Jiang, A dispersion-dominated chromogenic strategy for colorimetric sensing of glutathione at the nanomolar level using gold nanoparticles, Small 11 (2015) 5510–5514.

[16] Z. Liu, X. Zhou, Y. Miao, Y. Hu, N. Kwon, X. Wu, J. Yoon, A reversible fluorescent probe for real-time quantitative monitoring of cellular glutathione, Angew. Chem. Int. Ed. 56 (2017) 5812–5816.

[17] A.B.E. Attia, G. Balasundaram, M. Moothanchery, U.S. Dinish, V. Bi R, Ntziachristos, M. Olivo, A review of clinical photoacoustic imaging: current and future trends, Photoacoustics 16 (2019) 100144.

[18] L.V. Wang, S. Hu, Photoacoustic tomography: in vivo imaging from organelles to organs, Science 335 (2012) 1458–1462.

[19] P.K. Upputuri, M. Pramanik, Photoacoustic imaging in the second near-infrared window: a review, J. Biomed. Opt. 24 (2019) 1–20.

[20] Y. Zhang, M. Jeon, L.J. Rich, H. Hong, J. Geng, Y. Zhang, S. Shi, T.E. Barnhart, P. Alexandridis, J.D. Huizinga, M. Seshadri, W. Cai, C. Kim, J.F. Lovell, Non-invasive multimodal functional imaging of the intestine with frozen micellar naphthalocyanines, Nat. Nanotechnol. 9 (2014) 631–638.

[21] J. Weber, P.C. Bear, S.E. Bohndiek, Contrast agents for molecular photoacoustic imaging, Nat. Methods 13 (2016) 639–650.

[22] Y. Wu, J. Chen, L. Sun, F. Zeng, S. Wu, A nanoprobe for diagnosing and mapping lymphatic metastasis of tumor using 3D multispectral optoacoustic tomography owing to aggregation/deaggregation induced spectral change, Adv. Funct. Mater. 29 (2019) 1807960.

[23] S.R. Kothapalli, G.A. Sonn, J.W. Choe, A. Nikoozadeh, A. Bhuyan, K.K. Park, P. Cristman, R. Fan, A. Moini, B.C. Lee, J. Wu, T.E. Carver, D. Trivedi, L. Shiiba, I. Steinberg, D.M. Huland, M.F. Rasmussen, J.C. Liao, J.D. Brooks, P.T. Khuri-Yakub, S.S. Gambhir, Simultaneous transrectal ultrasound and photoacoustic human prostate imaging, Sci. Transl. Med. 11 (2019), eaav2169.

[24] Z. Wang, M. Zhan, W. Li, C. Chu, D. Xing, S. Lu, X. Hu, Photoacoustic cavitation-ignited reactive oxygen species to amplify peroxynitrite burst by photosensitization-free polymeric nanocapsules, Angew. Chem. Int. Ed. 60 (2021) 4720–4731.

[25] D. Wang, M.M.S. Lee, W. Xu, G. Shan, X. Zheng, R.T.K. Kwok, J.W.Y. Lam, X. Hu, B. Z. Tang, Boosting non-radiative decay to do useful work: development of a multi-modality theranostic system from an AIEgen, Angew. Chem. Int. Ed. 58 (2019) 5628–5632.

[26] B.D. Zheng, J. Ye, Y.Y. Huang, M.T. Xiao, Phthalocyanine-based photoacoustic contrast agents for imaging and theranostics, Biomater. Sci. 9 (2021) 7811–7825.

[27] X. Zhen, K. Pu, X. Jiang, Photoacoustic imaging and photothermal therapy of semiconducting polymer nanoparticles: signal amplification and second near-infrared construction, Small 17 (2021), e2004723.

[28] V.P. Nguyen, Y. Li, J. Henry, W. Zhang, X. Wang, Y.M. Paulus, Gold nanorod enhanced photoacoustic microscopy and optical coherence tomography of choroidal neovascularization, ACS Appl. Mater. Interfaces 13 (2021) 40214–40228.

[29] T.A. Tabish, S. Dey, P. Mosca, M. Salimi, F. Palombo, P. Matousek, N. Stone, Smart gold nanostructures for light mediated cancer theranostics: combining optical diagnostics with photothermal therapy, Adv. Sci. 7 (2020) 1903441.

[30] A. de la Zerda, C. Zavaleta, S. Keren, S. Vaithilingam, S. Bodapati, Z. Liu, J. Levi, B. Smith, T.-J. Ma, O. Oralkan, Z. Cheng, X. Chen, H. Dai, B.T. Khuri-Yakub, S. S. Gambhir, Carbon nanotubes as photoacoustic molecular imaging agents in living mice, Nat. Nanotechnol. 3 (2008) 557–562.

[31] M. Gifani, D.J. Eddins, H. Kosuge, Y. Zhang, S.L.A. Paluri, T. Larson, N. Leeper, L. A. Herzenberg, S.S. Gambhir, M.V. McConnell, E.E.B. Ghosn, B.R. Smith, Ultra-selective carbon nanotubes for photoacoustic imaging of inflamed atherosclerotic plaques, Adv. Funct. Mater. 31 (2021) 2101005.

[32] X. Ling, Z. Jin, Q. Jiang, X. Wang, B. Wei, Z. Wang, Y. Xu, T. Ca, J.W. Engle, W. Cai, C. Su, Q. He, Engineering biocompatible TeSe$_x$ nano-alloys as a versatile theranostic nanoplatform, Natl. Sci. Rev. 8 (2021) nwaa156.

[33] Y. Zhu, Y. Wang, G.R. Williams, L. Fu, J. Wu, H. Wang, R. Liang, X. Weng, M. Wei, Multicomponent transition metal dichalcogenide nanosheets for imaging-guided photothermal and chemodynamic therapy, Adv. Sci. 7 (2020) 2000272.

[34] J. Zhao, L. Zhang, Y. Qi, K. Liao, Z. Wang, M. Wen, D. Zhou, NIR laser responsive nanoparticles for ovarian cancer targeted combination therapy with dual-modal imaging guidance, Int. J. Nanomed. 16 (2021) 4351–4369.

[35] Z. Yang, Y. Dai, C. Yin, Q. Fan, W. Zhang, J. Song, G. Yu, W. Tang, W. Fan, B. C. Yung, J. Li, X. Li, X. Li, Y. Tang, X. Huang, J. Song, X. Chen, Activatable semiconducting theranostics: simultaneous generation and ratiometric photoacoustic imaging of reactive oxygen species in vivo, Adv. Mater. 30 (2018), e1707509.

[36] S. Wang, L. Zhang, J. Zhao, M. He, Y. Huang, S. Zhao, A tumor microenvironment-induced absorption red-shifted polymer nanoparticle for simultaneously activated photoacoustic imaging and photothermal therapy, Sci. Adv. 7 (2021), eabe3588.

[37] Z. Yang, B. Gu, C. Jiang, L. Zhang, Q. Liu, S. Song, A pH-responsive photoacoustic imaging probe for tumor pH imaging in vivo based on polyaniline-bovine serum albumin, Nanomedicine 33 (2021) 102356.

[38] S.H. Piao, M. Bhaumik, A. Maitycde, H. Jin Cho, Polyaniline/Fe composite nanofiber added softmagnetic carbonyl iron microsphere suspension and its magnetorheology, J. Mater. Chem. C 3 (2015) 1861–1868.

[39] J. Yang, J. Choi, D. Bang, E. Kim, E.-K. Lim, H. Park, J.-S. Suh, K. Lee, K.-H. Yoo, E.-K. Kim, Y.-M. Huh, S. Haam, Convertible organic nanoparticles for near-infrared photothermal ablation of cancer cells, Angew. Chem. Int. Ed. 50 (2011) 441–444.

[40] J. Li, H. Xiao, S.J. Yoon, C. Liu, D. Matsuura, W. Tai, L. Song, M. O'Donnell, D. Cheng, X. Gao, Functional photoacoustic imaging of gastric acid secretion using pH-responsive polyaniline nanoprobes, Small 34 (2016) 4690–4696.

[41] S. Wang, L. Zhang, J. Zhao, M. He, Y. Huang, S. Zhao, Sci. Adv. 7 (2021), eabe3588.